



### Key Points:

- Prior Carrington event analyses attributed the  $\Delta H$  perturbation observed on Earth to various causes, with debate on which dominated
- Using MHD simulations, we compute how currents in various systems and geospace regions contribute to  $\Delta H$
- Rather than a dominant contributor, we find that multiple current systems and regions contribute with the same order of magnitude

### Correspondence to:

R. S. Weigel,  
rweigel@gmu.edu

### Citation:

Thomas, D., Weigel, R. S., Pulkkinen, A., Schuck, P. W., Welling, D. T., & Ngwira, C. M. (2024). What drove the Carrington event? An analysis of currents and geospace regions. *Journal of Geophysical Research: Space Physics*, 129, e2024JA032556. <https://doi.org/10.1029/2024JA032556>

Received 28 FEB 2024

Accepted 13 JUN 2024

## What Drove the Carrington Event? An Analysis of Currents and Geospace Regions

Dean Thomas<sup>1</sup> , Robert S. Weigel<sup>1</sup> , Antti Pulkkinen<sup>2</sup> , Peter W. Schuck<sup>2</sup>, Daniel T. Welling<sup>3</sup> , and Chigomezyo M. Ngwira<sup>4</sup>

<sup>1</sup>Space Weather Lab, Department of Physics and Astronomy, George Mason University, Fairfax, VA, USA, <sup>2</sup>Heliophysics Science Division, NASA Goddard Space Flight Center, Greenbelt, MD, USA, <sup>3</sup>Climate and Space Sciences Engineering, University of Michigan, Ann Arbor, MI, USA, <sup>4</sup>Department of Physics, Catholic University of America, Washington, DC, USA

**Abstract** The 1859 Carrington event is the most intense geomagnetic storm in recorded history, and the literature provides numerous explanations for what drove the negative  $H$  perturbation on the Earth. There is debate on what dominated the event. Our analysis shows a combination of causes of similar orders of magnitude. Previous analyses generally rely upon the observed  $H$  perturbation at Colaba, India; historic newspaper reports; and empirical models. We expand the analysis using two Space Weather Modeling Framework simulations to examine what drove the event. We compute contributions from currents and geospace regions to the northward  $B$  field on Earth's surface,  $B_N$ . We examine magnetospheric currents parallel and perpendicular to the local  $B$  field, ionospheric currents, and gap region field-aligned currents (FACs). We also evaluate contributions from the magnetosheath, near-Earth, and neutral sheet regions. A combination of currents and geospace regions significantly contribute to  $B_N$  on the Earth's surface, changing as the storm evolves. At storm onset, magnetospheric currents and gap-region FACs dominate in the equatorial region. At auroral latitudes, gap-region FACs and ionospheric currents are the largest contributors. At storm peak, azimuthal magnetospheric currents and gap-region FACs dominate at equatorial latitudes. Gap-region FACs and ionospheric currents dominate in the auroral zone, down to mid-latitudes. Both the magnetosheath and FACs contribute at storm peak, but are less significant than that from the near-Earth ring current. During recovery, the near-Earth ring current is the largest contributor at equatorial latitudes. Ionospheric currents and gap-region FACs dominate in the auroral zone.

### 1. Introduction

The 2 September 1859, Carrington event (Carrington, 1859) was an exceptionally strong geomagnetic disturbance. Although geomagnetic observatories existed then, these systems had limitations that hinder analysis of the event (Blake et al., 2020). Measurements were taken manually with limited manpower and consequently had long gaps between measurements (Curto, 2019). For example, measurements were taken once per hour at the Madras Observatory, except on Sundays when no measurements were taken (Jacob, 1884). This is a concern because even hourly measurements can miss rapid variations in geomagnetic storms (Viljanen et al., 2014). Although some sites had continuously recording magnetograms, such as in British observatories (Boteler, 2019), geomagnetic disturbances could exceed their operational limits. For example, the horizontal magnetometer in Rome, Italy had an operational range of  $\sim 300$  nT, which is well below the range of the Carrington event (Blake et al., 2020).

The horizontal magnetogram data from Colaba, India are commonly used in analyses of the Carrington event (B. T. Tsurutani et al., 2003; Kumar et al., 2015). Unlike other data sets, these measurements were taken with a relatively high sampling rate (beginning with one measurement every hour and increasing to every 5 min). The Colaba measurements do not appear to go off-scale during the measurement period. The horizontal  $B$  field,  $B_H$ , decreased by  $\sim 1,600$  nT over 2 hr, then rapidly increased by  $\sim 1,250$  nT over 20 min. This rate and magnitude of change are unique among low-latitude  $B_H$  measurements.

Various hypotheses for  $B_H$  observed at Colaba have been suggested.

- Green and Boardsen (2006) noted that “the large negative  $D_{st}$  values of the [Bombay] magnetometer occurred during a time of rapid equatorward expansion of the aurora to the incredibly low geomagnetic latitudes ... Ground-based auroral electrojet magnetometer measurements of 1,760 nT, although large, are much more in line with what is measured from auroral currents than the ring current.”

2. Similarly, Cliver and Dietrich (2013) stated, “Various lines of evidence reviewed here … indicate that a similar auroral-induced (negative) bay contributed to the negative spike in the Colaba trace in 1859.”
3. In contrast, Siscoe et al. (2006) concluded “…that it is possible to interpret the Bombay magnetogram as having been produced by the magnetospheric currents.”
4. Cid et al. (2015) stated that “…the main cause of the large drop in  $H$  recorded at Colaba during the Carrington storm was not the ring current but field-aligned currents (FACs).”
5. Blake et al. (2021) stated “…magnetospheric currents adjacent to the near-Earth magnetopause and strong Region 1 field-aligned currents are the main contributors to the large Colaba  $B_H$ .”
6. Recently, there has been a discussion on the relative importance of FAC contributions. Ohtani (2022) stated “similarities to the Halloween storm magnetic depression suggest that the Colaba  $H$  depression was also caused by the dayside R1-sense wedge current system.” Whereas, B. T. Tsurutani et al. (2023) viewed this as “highly improbable … [rather] the cause of the Carrington storm was most probably a  $B_z \sim -90$  nT component inside an interplanetary magnetic cloud.”
7. Finally, Keika et al. (2015) proposed “…that the [ring current] flow-out effect plays a significant role in the rapid recovery of the Carrington storm.”

Because the literature has diverse views, we try to resolve which current systems and geospace regions are responsible for the magnetic signature observed at Colaba and elsewhere on the Earth's surface. Due to the limitations of the historic observations, we use results from Space Weather Modeling Framework (SWMF; Tóth et al., 2005; Gombosi et al., 2021; Welling, 2019) simulations to calculate contributions to the north  $B$  field ( $B_N$ ) on the Earth's surface:

1. From magnetospheric, ionospheric, and gap region currents; and
2. From the magnetosheath, neutral sheet, and near-Earth regions.

Our objective is to get a new perspective on the question using a quantitative approach to understand which current systems and regions dominate the event. A limitation of this approach is that we do not have measured solar wind data from the Carrington event to provide as input into a SWMF simulation, and we must use assumed values based on experience with other storms.

In analyzing the SWMF simulation results, we observe multiple current systems and geospace regions providing contributions of similar magnitude. And most proposed causes (Blake et al., 2021; Cid et al., 2015; Cliver & Dietrich, 2013; Green & Boardsen, 2006; Siscoe et al., 2006) play a significant role.

In the following sections, we provide the details of our analysis. In Section 2, we describe two sets of solar wind conditions applicable to the Carrington event, which we use in SWMF simulations. In Section 3, we discuss the details of our methodology. This section discusses how SWMF results are analyzed to isolate contributions from specific currents and geospace regions to the magnetic field measured on the Earth's surface. In Section 4, we examine these contributions, first at Colaba, India and then across the Earth's surface. We identify which currents and geospace regions dominate changes in the magnetic field. This analysis highlights the trends observed in the results and how the contributions evolve over time. And finally, in Section 5, we summarize our conclusions.

## 2. Solar Wind Conditions

We examine two Carrington-like solar wind scenarios. Scenario 1 is from Blake et al. (2021) and Scenario 2 is from Ngwira et al. (2014). These scenarios provide different approaches for recreating Carrington-like conditions.

The authors of Scenario 1 attempted to replicate the Carrington event by adjusting the solar wind inputs such that the simulated  $B$  field at Colaba was similar to that observed. The historic Colaba  $B_H$  time series was used as a template for the shape of the solar wind parameters: interplanetary magnetic field, velocity, particle density, and temperature. The objective was to produce a fast solar wind that would cause a high ram pressure and lead to a large magnetopause compression. Each solar wind parameter was scaled to peak at ~06:30 GMT when the Colaba  $B_H$  was at its most extreme. Figure 1 shows the solar wind conditions used in Scenario 1.

The authors of Scenario 2 attempted to create a “Carrington-type” event rather than replicating the event. The solar wind parameters were estimated to create a strong geomagnetic perturbation, and a portion of the Halloween 2003 storm was superimposed onto the solar wind parameters to introduce realistic solar wind fluctuations. For the

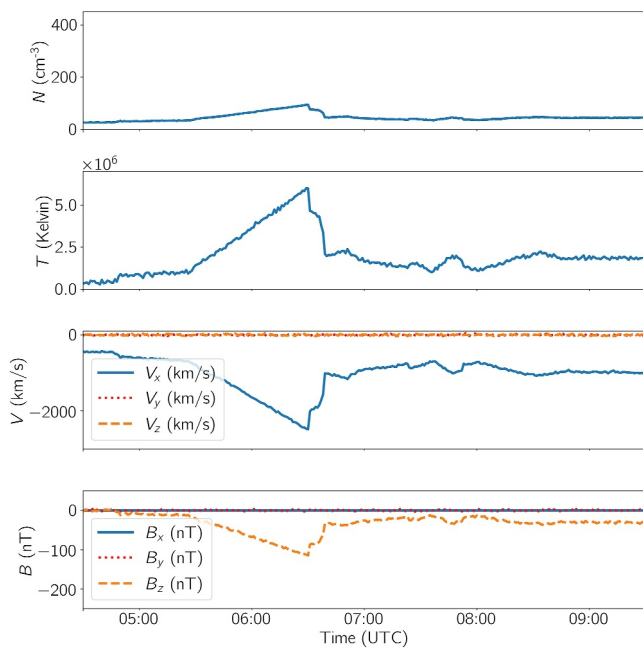


**Figure 1.** Scenario 1 solar wind conditions from Blake et al. (2021).

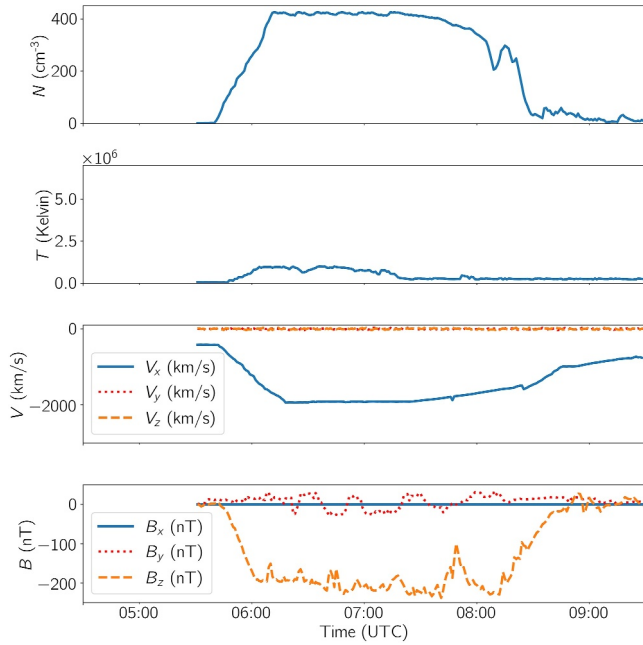


**Figure 2.** Scenario 2 solar wind conditions from Ngwira et al. (2014).

analysis in this paper, the solar wind conditions are time-shifted 5.5 hr so that Colaba is at approximately the same local time as it is in the Scenario 1 when the storm peaks. Figure 2 shows the solar wind conditions used in Scenario 2.

The solar wind conditions in these scenarios are substantially different, allowing the analysis to consider how sensitive the results are to different solar winds. In Scenario 1, the large excursion in the solar wind lasts just over 1 hr (from  $\sim$ 05:30 to  $\sim$ 06:45), but in Scenario 2, it lasts about 3 hr (from  $\sim$ 05:45 to  $\sim$ 08:45). And the magnitude of the changes in the solar wind are significantly different between the two scenarios. For example, the maximum temperature,  $T$ , is  $\sim$ 5 times larger in the first scenario compared to the second. Additional differences are seen in other parameters.

To provide context for the solar wind conditions in these scenarios, we consider the range of values seen in a modern superstorm - the Halloween 2003 storm. B. Tsurutani et al. (2006) show a peak solar wind speed of  $\sim$ 2,100 km/s, a peak temperature of  $\sim$ 1.4  $\times$  10<sup>7</sup> K, a peak density of  $\sim$ 25 per cm<sup>3</sup>, and a  $B_z$  ranging between  $\sim$ -60 to +40 nT.

### 3. Methodology

Our methodology involves calculating and analyzing contributions to the northward  $B$  field on Earth's surface,  $B_N$ , from currents in geospace regions and systems. We examine the magnetospheric currents parallel and perpendicular to the local  $B$  field, ionospheric currents, and gap region FACs. We also evaluate contributions from the magnetosheath, near-Earth, and neutral sheet current systems.

We focus on what drove  $B_H$  and note that  $B_N$  is the dominant contributor to  $B_H$ . In the scenarios we examine, the average  $|B_H/B_N|$  near Colaba is  $\approx$  1. As the dominant contributor and a vector, we use  $B_N$  rather than the scalar  $B_H$  in our analysis.

The results from both scenarios are from the SWMF (Tóth et al., 2005). Runs were executed at NASA's Community Coordinated Modeling Center (CCMC; Hesse et al., 2001).

We use the Biot-Savart Law and the current density,  $\mathbf{j}$ , to calculate the  $B_N$  contributions from magnetospheric, gap-region, and ionospheric currents on the Earth's surface.

#### 3.1. Magnetospheric Currents

$B_N$  contributions from magnetospheric currents are divided into components parallel and perpendicular to the local  $B$  field.

$$j_{\parallel} = \mathbf{j} \cdot \frac{\mathbf{B}}{|\mathbf{B}|}$$

$$\mathbf{j}_{\perp} = \mathbf{j} - j_{\parallel} \frac{\mathbf{B}}{|\mathbf{B}|}$$

We further decompose  $j_{\perp}$  into two components:

$$j_{\perp\phi} = \mathbf{j}_{\perp} \cdot \hat{\phi}$$

$$\Delta j_{\perp} = |\mathbf{j}_{\perp} - j_{\perp\phi} \hat{\phi}|$$

The dominant  $B_N$  contributions generally are from the  $j_{\parallel}$  and  $j_{\perp\phi}$  components. The contributions from the  $\Delta j_{\perp}$  component are typically small. One component,  $j_{\perp\phi}$ , is azimuthally-directed and can lead to a ring current.

#### 3.2. Magnetospheric Regions

We also consider which magnetospheric regions provide the largest contributions to  $B_N$ . Figure 3 is taken from Scenario 1 at 06:00 (UTC) and illustrates the identification of the bow shock, magnetopause, and neutral sheet. The boundary conditions used to identify them are (Baumjohann & Treumann, 2012):

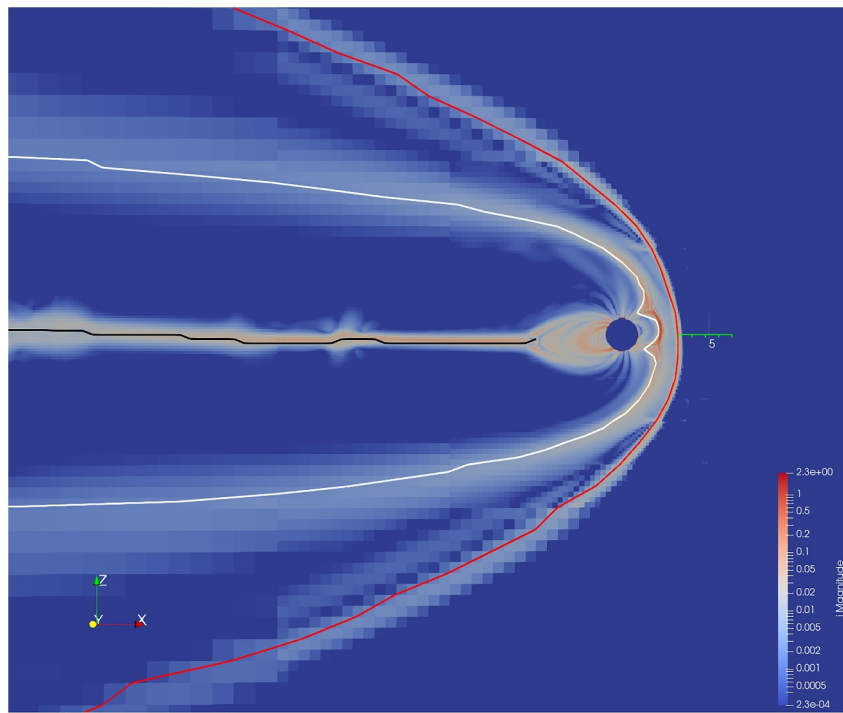


**Figure 3.** Identification of bow shock (red line), magnetopause (white line), and neutral sheet (black line) for Scenario 1 at 06:00 (UTC). Colormap is  $\log_{10}|j|$ , with  $j$  having units of  $(\mu\text{A}/\text{m}^2)$ . Green ruler is  $5R_E$  long.

1. Bow shock: solar wind speed normal to the bow shock,  $u_{BS\perp}$ , becomes submagnetosonic ( $u_{BS\perp} < c_{MS}$  where  $c_{MS}$  is the magnetosonic speed).
2. Magnetopause: magnetic pressure due to tangential  $\mathbf{B}$  field,  $p_{\text{mag}}$ , equals thermal pressure,  $p_{\text{thermal}}$ , plus dynamic ram pressure due to solar wind normal to the magnetopause,  $p_{\text{dyn}}$  ( $p_{\text{mag}} = p_{\text{thermal}} + p_{\text{dyn}}$ ).
3. Neutral sheet:  $\mathbf{B}$  field switches direction ( $B_x = 0$ ) in the region anti–sunward of the Earth and inside of the magnetopause.

Calculations are performed in geocentric solar magnetospheric (GSM) coordinates. Additional details are given in the appendix.

Using the locations of the bow shock, magnetopause, and neutral sheet, the SWMF grid is divided into four regions:

1. The magnetosheath includes the grid points between the magnetopause and the bow shock. In examining the current density near the bow shock, we observe a thin current layer covering the sunward side of the bow shock (Figure 3). We include this current in the magnetosheath by including points within  $0.5R_E$  Bsunward of the bow shock.
2. The near–Earth region is within  $6.6R_E$  of the Earth's center and anti–sunward of the magnetopause. The  $6.6R_E$  criteria is based on Ganushkina et al. (2018) noting the tail current is outside of  $6.6R_E$  and Le et al. (2004) observing that ring currents are within  $\sim 7R_E$ .
3. The neutral sheet region is within  $\pm 3R_E \hat{z}$  of the neutral sheet, outside of the near–Earth region, and anti–sunward of Earth. This region includes both the plasma sheet (PS) and plasma sheet boundary layer (PSBL), and the  $\pm 3R_E \hat{z}$  criteria is based on SPDF - Satellite Situation Center Web (SSCWeb) (2023) limits.
4. Any remaining points from the SWMF grid are placed into the “other” region.

### 3.3. Gap Region, and Ionospheric Currents

In addition to magnetospheric currents, we examine contributions from gap–region FACs and ionospheric Pedersen and Hall currents. The gap region is between the ionosphere and  $1.8R_E$  in Scenario 1 and the ionosphere and  $1.5R_E$  in Scenario 2. In MHD simulations, the currents are assumed to be field–aligned in the gap region to

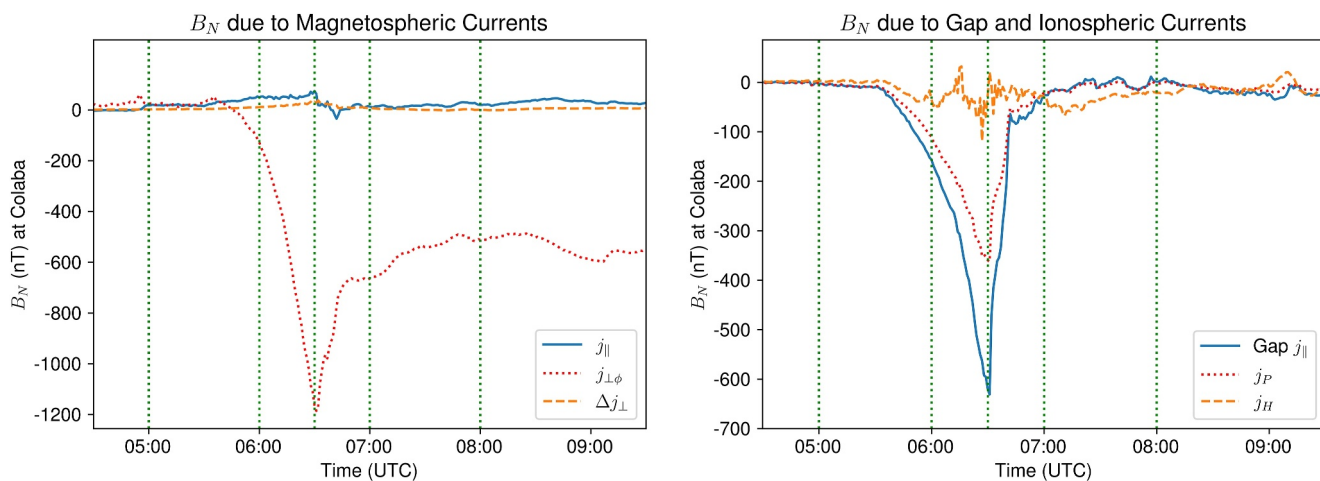


**Figure 4.** Scenario 1:  $B_N$  contributions at Colaba from magnetospheric, gap, and ionospheric currents. Vertical dotted lines are times selected for additional analysis. The total  $B_N$  contribution at Colaba is the sum of the contributions from the six currents.

reduce simulation time. (Near Earth, the Alfvén velocity (Yu et al., 2010) becomes large. To avoid small time steps, the MHD simulation assumes field-aligned currents.)

#### 4. Results

Figures 4 and 5 show the contributions that the magnetospheric currents, gap-region FAC, and ionospheric Pedersen ( $j_P$ ) and Hall ( $j_H$ ) currents make to  $B_N$  on the Earth's surface at Colaba. The total  $B_N$  contribution at Colaba is the sum of the contributions from the six currents.  $B_N$  is minimum at  $\sim$ 06:30 in Scenario 1 and  $\sim$ 07:30 in Scenario 2.

Important overarching conclusions follow from Figures 4 and 5. The relative magnitude of the  $B_N$  contributions is similar in both scenarios. For magnetospheric currents,  $j_{\perp\phi}$  dominates in both scenarios. The  $j_{\parallel}$  and  $\Delta j_{\perp}$  contributions are much smaller. Similarly, we see the same ordering of gap-region and ionospheric contributions in both scenarios. The gap-region FAC contribution is the most negative, followed by ionospheric Pedersen currents. Ionospheric Hall currents are the most positive, with Scenario 2 having larger Hall  $B_N$  contributions than Scenario 1.

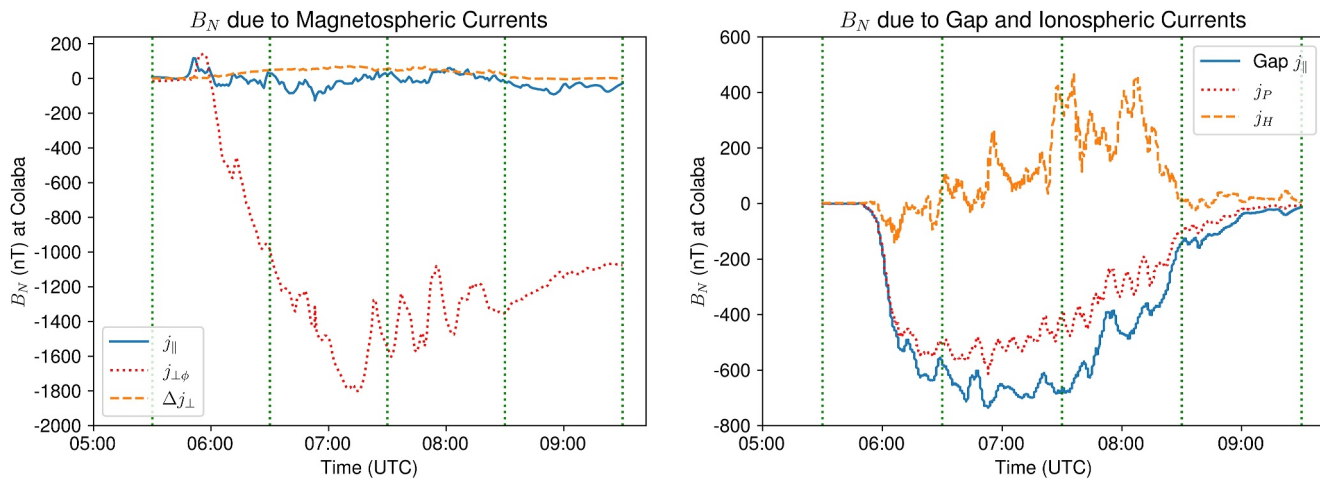


**Figure 5.** Scenario 2:  $B_N$  contributions at Colaba from magnetospheric, gap, and ionospheric currents. Vertical dotted lines are times selected for additional analysis. The total  $B_N$  contribution at Colaba is the sum of the contributions from the six currents.

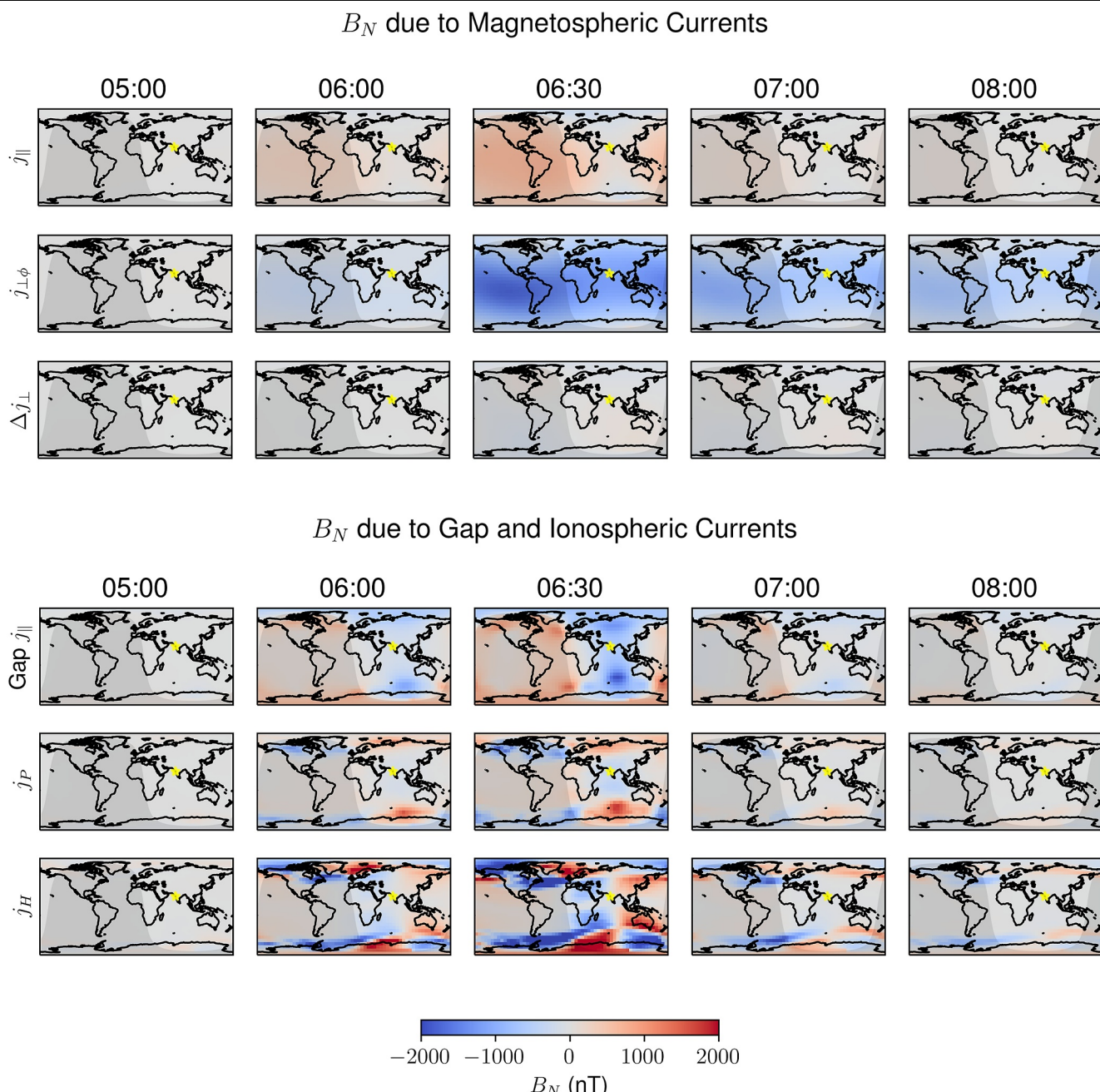


**Figure 6.** Scenario 1:  $B_N$  contributions from magnetospheric currents, gap region FAC, and ionospheric Pedersen and Hall currents. Each column represents a different time identified in Figure 4. The yellow star shows the location of Colaba, and the shading indicates the day/night boundary.

Overall, the magnetospheric  $j_{\perp\phi}$ , gap-region FACs, and ionospheric Pedersen currents drive the negative deviation in  $B_N$  at Colaba. We also note that they are of the same order of magnitude. Although there is uncertainty in the assumed solar wind conditions, the consistent results from the different solar wind conditions in the two scenarios indicate these three currents are significant contributors.

We expand this analysis from a single point at Colaba to the entire Earth's surface. The analysis focuses on specific times that illustrate the evolution of  $B_N$ . For Scenario 1, we select five times—05:00 before the  $B_N$  decrease begins, 06:00 during the growth phase, 06:30 at  $B_N$  minimum, 07:00 during the recovery phase, and 08:00 when the recovery is well advanced (vertical dotted lines in Figure 4). Similarly, for Scenario 2, we select

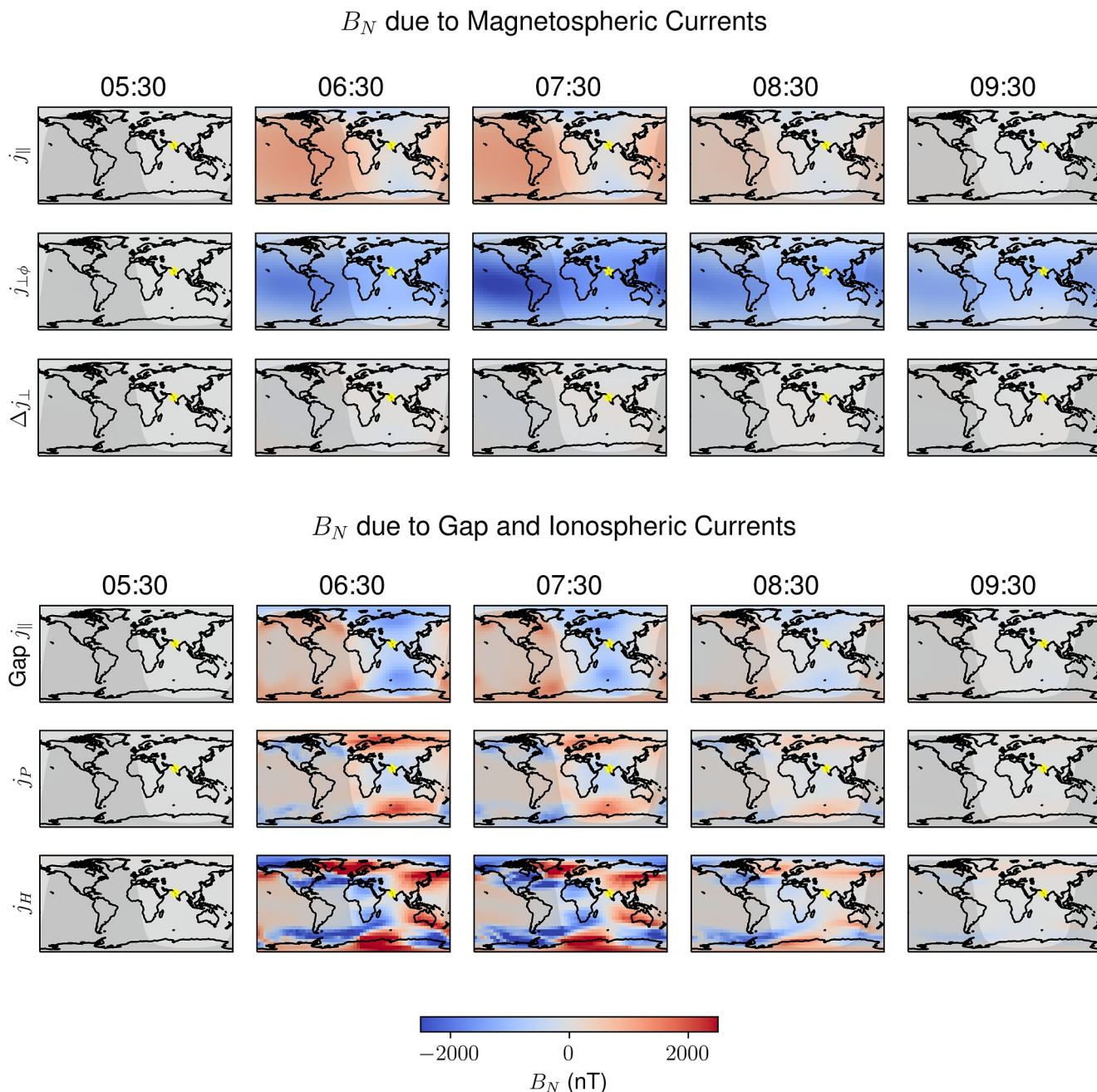


**Figure 7.** Scenario 2:  $B_N$  contributions from magnetospheric currents, gap region FAC, and ionospheric Pedersen and Hall currents. Same format as Figure 6. Times are identified in Figure 5.

05:30, 06:30, 07:30, 08:30, and 09:30 for further analysis (vertical dotted lines in Figure 5). For each scenario, heatmaps illustrating the evolution of  $B_N$  across the Earth's surface are shown in Figures 6 and 7. The columns in each figure correspond to the selected times, and the rows correspond to the magnetospheric, gap, and ionospheric currents discussed above.

Both figures show a similar evolution of  $B_N$ , as seen through the similar color patterns:

1. At storm onset (06:00 in Figures 6 and 06:30 in Figure 7), in the equatorial region, magnetospheric currents along with gap-region FACs dominate  $B_N$  contributions. At auroral latitudes, gap-region FACs and ionospheric currents dominate.

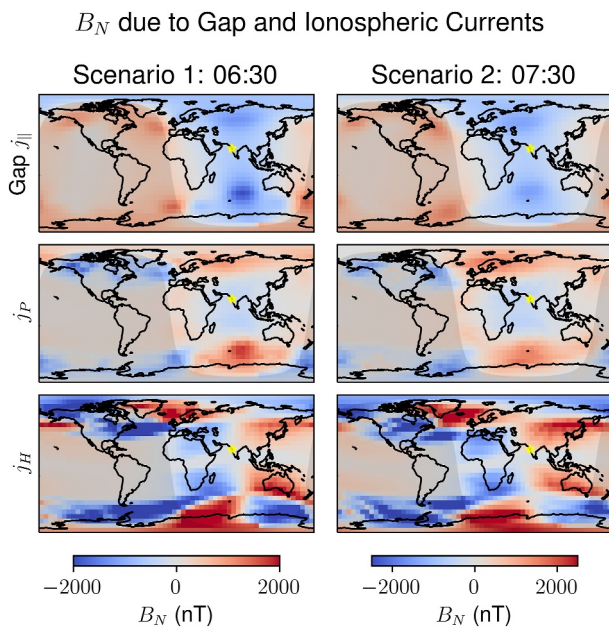


**Figure 8.** Comparison of heatmaps from Scenario 1 at 06:30 (UTC) and Scenario 2 at 07:30 (UTC), near the storm peak. These heatmaps are taken, unchanged, from Figures 6 and 7. Although the solar wind conditions are different, the similarities between the heatmaps are apparent.

2. At the peak (06:30 in Figure 6 and 07:30 in Figure 7), azimuthal magnetospheric currents and gap-region FACs dominate at equatorial latitudes. Gap-region FACs and ionospheric currents dominate in the auroral zone, down to mid-latitudes.
3. As shown below, the magnetosheath is a strong contributor. Both the magnetosheath and FACs contribute at storm peak, but they are less significant than magnetospheric  $j_{\perp\phi}$ , which we will show is a ring current.
4. During recovery (07:00 and 08:00 in Figure 6; 08:30 and 09:30 in Figure 7), the ring current is the largest contributor at equatorial latitudes. As Keika et al. (2015) suggested, ring current relaxation is driving recovery. In contrast, ionospheric currents and, to a lesser extent, gap-region FACs are the dominant contributors in the auroral zone.

The heatmaps from the scenarios have numerous similarities, strengthening the conclusions that we draw. As an example, Figure 8 compares gap-region and ionospheric current heatmaps. The left column is taken from Figure 6, and the right is from Figure 7. The two extracts are near the storm peaks, 06:30 for Scenario 1 and 07:30 for Scenario 2. The heatmaps contain features common to both scenarios, and the similarities are apparent. Comparisons of other parts of Figures 6 and 7 show other similarities. Because the solar wind conditions for the two scenarios are different, these commonalities suggest that the conclusions that we draw from the two scenarios are robust.

To further understand the role of magnetospheric currents, we divide the SWMF grid into four regions, which leads to additional conclusions. The regions are defined above: magnetosheath, near Earth, neutral sheet, and

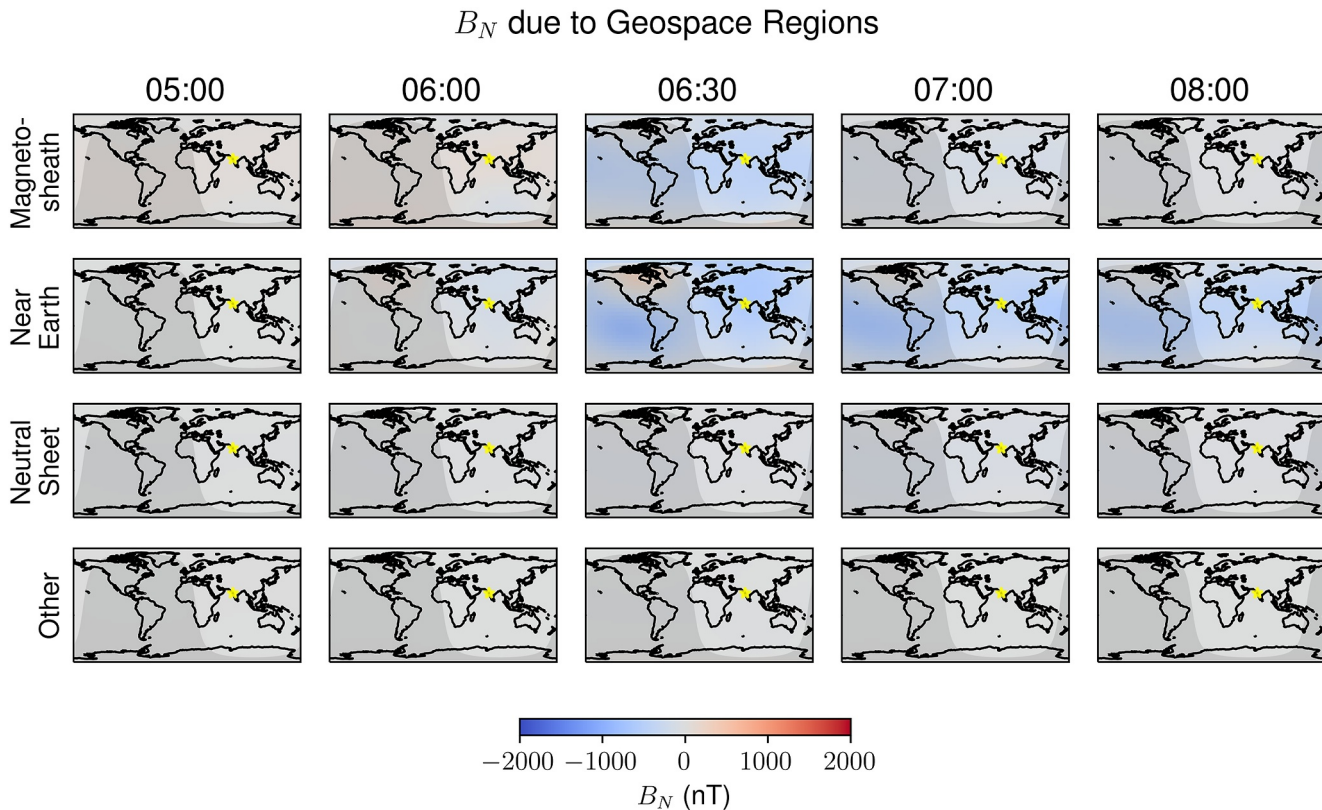


**Figure 9.** Scenario 1:  $B_N$  contributions from magnetospheric currents in the magnetosheath, near Earth, neutral sheet, and other regions. Same format as Figure 6. Times are identified in Figure 4.

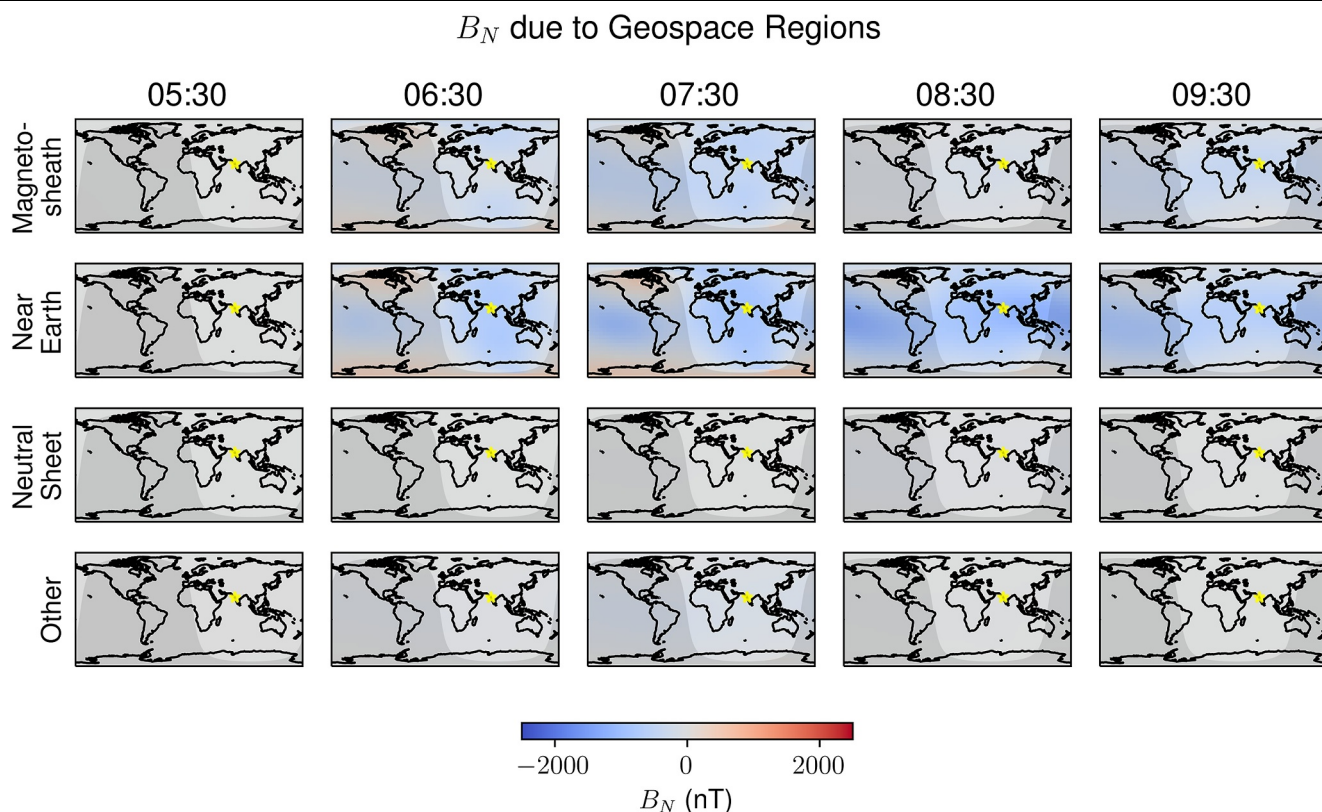


**Figure 10.** Scenario 2:  $B_N$  contributions from magnetospheric currents in the magneto-sheath, near Earth, neutral sheet, and other regions. Same format as Figure 6. Times are identified in Figure 5.

other. The  $B_N$  contributions from these regions in Scenarios 1 and 2 are shown in Figures 9 and 10. Magneto-sheath and near-Earth regions are the primary contributors to  $B_N$  as the excursion starts (06:00 in Figures 9 and 06:30 in Figure 10), with the near-Earth region providing the largest contributions. The neutral sheet and other regions do not contribute significantly. As  $B_N$  recovers (07:00 and 08:00 in Figure 9 and 08:30 and 09:30 in Figure 10), the near-Earth region is the dominant contributor. As discussed earlier, at the storm's peak and during recovery, we observe large magnetosphere  $j_{\perp\phi}$  contributions, which we see here are near Earth. Consequently, ring currents are significant.

## 5. Summary and Conclusions

Our analysis shows that the Carrington event was due to a combination of magnetospheric and ionospheric currents. With multiple currents and geospace regions providing  $B_N$  contributions of the same order of magnitude. Since the Carrington event pumped a tremendous amount of energy into the Earth's magnetosphere, it is not surprising that multiple pathways are needed to restore equilibrium.

Because our conclusions are insensitive to the solar wind conditions, they should be applicable to a range of superstorms comparable to the Carrington event. As noted previously, the solar wind conditions (Figures 1 and 2) are substantially different between the two scenarios examined, but the conclusions drawn from both scenarios are consistent. Consequently, they should be relevant to a range of superstorms that produce large changes in  $B_N$  on the Earth's surface. Whether these conclusions are applicable to smaller storms is unclear because the scenarios involve only Carrington-like events.

Such superstorms are expected to include  $B_N$  contributions, of the same-order-of-magnitude, from multiple magnetospheric and ionospheric currents. Furthermore, as a superstorm progresses, we expect the  $B_N$  contributions to evolve similarly to the evolution observed in this analysis.

Shortly after the onset of the high-pressure solar wind peak in the scenarios, we see significant changes to  $B_N$ . At storm onset, magnetospheric FACs and azimuthal currents, gap region FACs, and ionospheric Pedersen and Hall currents contribute. As the storm evolves, magnetospheric ring currents dominate in the equatorial regions, and gap region FAC and ionospheric Pederson and Hall currents dominate in the auroral regions.

As noted in Section 1, Green and Boardsen (2006), Cliver and Dietrich (2013), Cid et al. (2015), Siscoe et al. (2006), Cid et al. (2015), and Blake et al. (2021) proposed various factors as driving the Carrington event. Overall, most of the causes suggested in the literature play a role.

The literature examines both ionospheric (Cliver & Dietrich, 2013; Green & Boardsen, 2006) and magnetospheric currents (Siscoe et al., 2006), with discussion on which is more significant. Our analysis indicates that both ionospheric and magnetospheric currents make significant contributions to  $B_N$ . The contributions are of the same order of magnitude with magnetospheric contributions at Colaba being larger.

FAC in the magnetosphere and the gap region play an important role (Cid et al., 2015; Ohtani, 2022), although they are not as large as other contributors. The magnitude of the magnetosheath contributions is smaller than contributions from the near-Earth region, consistent with other observations (Blake et al., 2021).

Ohtani (2022) and B. T. Tsurutani et al. (2023) debated the significance of FACs. While gap-region FACs are not the dominate contributor at Colaba, they are not a minor contributor and are the same order of magnitude as magnetospheric and Pedersen contributions.

In addition, during recovery, azimuthal magnetospheric currents in the near-Earth region are significant as  $B_N$  stabilizes after the event (Keika et al., 2015).

## Appendix A: Magnetospheric Regions Methodology

We use an iterative approach to find the bow shock and magnetopause because we need their respective functional forms to determine the normals used in the boundary conditions defined in Section 3.2. In the first iteration, we assume paraboloid functional representations of the bow shock and magnetopause. From these, we calculate normals and use the boundary conditions to create numerical estimates of the bow shock and magnetopause locations. With the updated estimates, we recalculate the normals and repeat the process until convergence. In the discussion below, all positions are in GSM.

For the bow shock, we initially assume a one-parameter paraboloid (Formisano, 1979), whose width, measured at the Earth along the  $y$ - $z$  axes, is 4 times the subsolar distance from the Earth to the bow shock,  $x_{BS}$ :

$$x = x_{BS} - \frac{y^2 + z^2}{4x_{BS}}.$$

The subsolar distance is determined by the bow shock boundary condition and the assumption that the bow shock lies along the  $x$ -axis with normal  $(1, 0, 0)$ . In later iterations, we use a two-parameter ( $A$  and  $B$ ) paraboloid:

$$x = x_{BS} + Ay^2 + Bz^2.$$

For the magnetopause, we also initially assume a one-parameter paraboloid:

$$x = x_{MP} - \frac{y^2 + z^2}{4x_{MP}},$$

where  $x_{MP}$  is the subsolar distance from the Earth to the magnetopause and is determined similarly to  $x_{BS}$ . As with the bow shock, we assume the paraboloid's width along the  $y$ - $z$  axes is  $4x_{MP}$ . In later iterations, we use the Shue et al. (1997) equation,

$$r = x_{MP} \left( \frac{2}{1 + \cos \theta} \right)^\alpha,$$

where  $r$  is the radial coordinate,  $\theta$  is the angle between  $r$  and the Earth-Sun line, and  $\alpha$  is a fit parameter. The two formulations are linked. As shown in Narita et al. (2023), when  $\alpha = 1$ , the Shue et al. (1997) equation reduces to a paraboloid.

To find the iterative solutions, we generate a grid of lines parallel to the  $x$ -axis. Using the assumed shapes, we determine normals to the bow shock and the magnetopause. These normals and data from the SWMF simulations are used to calculate the quantities in the boundary conditions. Each line in the grid is followed from the Sun toward the Earth until we find the points where the bow shock and magnetopause boundary conditions are satisfied. These points provide an  $(x, y, z)$  grid for the bow shock and a similar grid for the magnetopause.

Using a two-parameter paraboloid for the bow shock and the Shue et al. (1997) equation for the magnetopause, the shapes are updated using a least-squares fit to the grids. Fitting the equations smooths the normals. Digital artifacts in SWMF data (e.g., when the grid changes size) create discontinuities in the normals. Smoothing is required to allow convergence.

We repeat the process using the normals from the updated fits to determine new estimates for the bow shock and magnetopause. The process is repeated until the solutions converge, generally in a few iterations. Visual checks confirm that the bow shock and magnetopause are found.

For the neutral sheet, we look for the region in the magnetotail where  $B_x = 0$ . We explore the region inside the magnetopause and anti-sunward of Earth. We create a grid of lines parallel to the  $z$ -axis and follow the lines from positive to negative  $z$ . In one pass, we identify the  $B_x = 0$  boundary.

## Data Availability Statement

The software used in this analysis can be found at Thomas (2024). The Scenario 1 data set is available at Blake (2021), and the Scenario 2 data set is at Ngwira (2014).

## Acknowledgments

This work was supported by NASA Grant 80NSSC20K0589 and carried out using the SWMF and BATS-R-US tools developed at the University of Michigan's Center for Space Environment Modeling (CSEM). The modeling tools are available through the University of Michigan for download under a user license; an open-source version is available at <https://github.com/MSTEM-QUDA>. In developing the algorithms in our software, we reviewed other software packages used to analyze SWMF results. Specifically, we reviewed magnetopost (Quaresima, 2023a), swmfio (Quaresima, 2023b), and CalcDeltaB (Rastätter et al., 2014). We also considered previous work examining dipole magnetic fields and currents near Earth (Chapman & Sugiura, 1956; Lotko, 2004; Willis & Young, 1987).

## References

- Baumjohann, W., & Treumann, R. A. (2012). *Basic space plasma physics*. Imperial College Press. <https://doi.org/10.1142/p850>
- Blake, S. P. (2021). CARR\_Scenario1. [Dataset]. CARR. Retrieved from [https://ccmc.gsfc.nasa.gov/results/viewrun.php?runnumber=CARR\\_Scenario1](https://ccmc.gsfc.nasa.gov/results/viewrun.php?runnumber=CARR_Scenario1)
- Blake, S. P., Pulkkinen, A., Schuck, P. W., Glocer, A., Oliveira, D. M., Welling, D. T., et al. (2021). Recreating the horizontal magnetic field at Colaba during the Carrington event with geospace simulations. *Space Weather*, 19(5). <https://doi.org/10.1029/2020sw002585>
- Blake, S. P., Pulkkinen, A., Schuck, P. W., Nevanlinna, H., Reale, O., Veenadhari, B., & Mukherjee, S. (2020). Magnetic field measurements from Rome during the August–September 1859 storms. *Journal of Geophysical Research: Space Physics*, 125(6). <https://doi.org/10.1029/2019ja027336>
- Boteler, D. H. (2019). A 21st century view of the March 1989 magnetic storm. *Space Weather*, 17(10), 1427–1441. <https://doi.org/10.1029/2019sw002278>
- Carrington, R. C. (1859). Description of a singular appearance seen in the Sun on September 1, 1859. *Monthly Notices of the Royal Astronomical Society*, 20(1), 13–15. <https://doi.org/10.1093/mnras/20.1.13>
- Chapman, S., & Sugiura, M. (1956). Arc-lengths along the lines of force of a magnetic dipole. *Journal of Geophysical Research*, 61(3), 485–488. <https://doi.org/10.1029/jz061i003p00485>
- Cid, C., Saiz, E., Guerrero, A., Palacios, J., & Cerrato, Y. (2015). A Carrington-like geomagnetic storm observed in the 21st century. *Journal of Space Weather and Space Climate*, 5, A16. <https://doi.org/10.1051/swsc/2015017>
- Cliver, E. W., & Dietrich, W. F. (2013). The 1859 space weather event revisited: Limits of extreme activity. *Journal of Space Weather and Space Climate*, 3, A31. <https://doi.org/10.1051/swsc/2013053>
- Curto, J. J. (2019). Uncertainty in hourly mean data from classical magnetometers. *Earth Planets and Space*, 71(1), 139. <https://doi.org/10.1186/s40623-019-1119-2>
- Formisano, V. (1979). Orientation and shape of the Earth's bow shock in three dimensions. *Planetary and Space Science*, 27(9), 1151–1161. [https://doi.org/10.1016/0032-0633\(79\)90135-1](https://doi.org/10.1016/0032-0633(79)90135-1)
- GANUSHKINA, N. Y., LIEMOHN, M. W., & DUBYAGIN, S. (2018). Current systems in the Earth's magnetosphere. *Reviews of Geophysics*, 56(2), 309–332. <https://doi.org/10.1002/2017rg000590>
- Gombosi, T. I., Chen, Y., Glocer, A., Huang, Z., Jia, X., Liemohn, M. W., et al. (2021). What sustained multi-disciplinary research can achieve: The space weather modeling framework. *Journal of Space Weather and Space Climate*, 11, 42. <https://doi.org/10.1051/swsc/2021020>
- Green, J. L., & Boardsen, S. (2006). Duration and extent of the great auroral storm of 1859. *Advances in Space Research*, 38(2), 130–135. <https://doi.org/10.1016/j.asr.2005.08.054>
- Hesse, M., Bellaire, P., & Robinson, R. (2001). Community coordinated modeling center: A new approach to space weather modeling. In *Proceedings of the space weather workshop: Looking towards a European space weather programme* (pp. 17–19).
- Jacob, W. S. (1884). *Magnetical observations made at the honorable East India Company's observatory at Madras observatory*. The Lawrence Asylum Press. Retrieved from [https://books.google.com/books/about/Magnetical\\_Observations\\_Made\\_at\\_the\\_Hono.html?id=TxVAAAAYAAJ](https://books.google.com/books/about/Magnetical_Observations_Made_at_the_Hono.html?id=TxVAAAAYAAJ)
- Keika, K., Ebihara, Y., & Kataoka, R. (2015). What caused the rapid recovery of the Carrington storm? *Earth Planets and Space*, 67(1), 65. <https://doi.org/10.1186/s40623-015-0234-y>

- Kumar, S., Veenadhari, B., Ram, S. T., Selvakumaran, R., Mukherjee, S., Singh, R., & Kadam, B. D. (2015). Estimation of interplanetary electric field conditions for historical geomagnetic storms. *Journal of Geophysical Research: Space Physics*, 120(9), 7307–7317. <https://doi.org/10.1002/2015ja021661>
- Le, G., Russell, C. T., & Takahashi, K. (2004). Morphology of the ring current derived from magnetic field observations. *Annales Geophysicae*, 22(4), 1267–1295. <https://doi.org/10.5194/angeo-22-1267-2004>
- Lotko, W. (2004). Inductive magnetosphere–ionosphere coupling. *Journal of Atmospheric and Solar-Terrestrial Physics*, 66(15–16), 1443–1456. <https://doi.org/10.1016/j.jastp.2004.03.027>
- Narita, Y., Toepfer, S., & Schmid, D. (2023). Magnetopause as conformal mapping. *Annales Geophysicae*, 41(1), 87–91. <https://doi.org/10.5194/angeo-41-87-2023>
- Ngwira, C. M. (2014). Chigomezyo\_Ngwira\_092112\_3a. [Dataset]. *Chigomezyo\_Ngwira*. Retrieved from [https://ccmc.gsfc.nasa.gov/results/viewrun.php?runnumber=Chigomezyo\\_Ngwira\\_092112\\_3a](https://ccmc.gsfc.nasa.gov/results/viewrun.php?runnumber=Chigomezyo_Ngwira_092112_3a)
- Ngwira, C. M., Pulkkinen, A., Kuznetsova, M. M., & Glocer, A. (2014). Modeling extreme “Carrington-type” space weather events using three-dimensional global MHD simulations. *Journal of Geophysical Research: Space Physics*, 119(6), 4456–4474. <https://doi.org/10.1002/2013ja019661>
- Ohtani, S. (2022). New insights from the 2003 Halloween storm into the Colaba 1600 nT magnetic depression during the 1859 Carrington storm. *Journal of Geophysical Research: Space Physics*, 127(9). <https://doi.org/10.1029/2022ja030596>
- Quaresima, G. (2023a). magnetopost. [Software]. *Github*. Retrieved from <https://github.com/GaryQ-physics/magnetopost>
- Quaresima, G. (2023b). swmfio. [Software]. *Github*. Retrieved from <https://github.com/GaryQ-physics/swmfio>
- Rastäter, L., Tóth, G., Kuznetsova, M. M., & Pulkkinen, A. A. (2014). CalcDeltaB: An efficient postprocessing tool to calculate ground-level magnetic perturbations from global magnetosphere simulations. *Space Weather*, 12(9), 553–565. <https://doi.org/10.1002/2014sw001083>
- Shue, J., Chao, J. K., Fu, H. C., Russell, C. T., Song, P., Khurana, K. K., & Singer, H. J. (1997). A new functional form to study the solar wind control of the magnetopause size and shape. *Journal of Geophysical Research*, 102(A5), 9497–9511. <https://doi.org/10.1029/97ja00196>
- Siscoe, G., Crooker, N., & Clauer, C. (2006). Dst of the Carrington storm of 1859. *Advances in Space Research*, 38(2), 173–179. <https://doi.org/10.1016/j.asr.2005.02.102>
- SPDF - Satellite Situation Center Web (SSCWeb). (2023). SPDF. Retrieved from [https://sscweb.gsfc.nasa.gov/users\\_guide/ssc\\_reg\\_doc.shtml](https://sscweb.gsfc.nasa.gov/users_guide/ssc_reg_doc.shtml)
- Thomas, D. (2024). dthoma6/deltaB: Carrington event paper (v1.0.0). [Software]. *Zenodo*. Retrieved from <https://doi.org/10.5281/zenodo.11409976>
- Tóth, G., Sokolov, I. V., Gombosi, T. I., Chesney, D. R., Clauer, C. R., De Zeeuw, D. L., et al. (2005). Space weather modeling framework: A new tool for the space science community. *Journal of Geophysical Research*, 110(A12). Retrieved from <https://doi.org/10.1029/2005JA011126>
- Tsurutani, B., Mannucci, A., Iijima, B., Guarnieri, F., Gonzalez, W., Judge, D., et al. (2006). The extreme Halloween 2003 solar flares (and Bastille Day, 2000 Flare), ICMEs, and resultant extreme ionospheric effects: A review. *Advances in Space Research*, 37(8), 1583–1588. <https://doi.org/10.1016/j.asr.2005.05.114>
- Tsurutani, B. T., Gonzalez, W. D., Lakhina, G. S., & Alex, S. (2003). The extreme magnetic storm of 1–2 September 1859. *Journal of Geophysical Research*, 108(A7). <https://doi.org/10.1029/2002ja009504>
- Tsurutani, B. T., Lakhina, G. S., & Hajra, R. (2023). Comments on “New insights from the 2003 Halloween storm into the Colaba 1600 nT magnetic depression during the 1859 Carrington storm” by S. ohtani (2022). *Journal of Geophysical Research: Space Physics*, 128(6). <https://doi.org/10.1029/2022ja031034>
- Viljanen, A., Myllys, M., & Nevanlinna, H. (2014). Russian geomagnetic recordings in 1850–1862 compared to modern observations. *Journal of Space Weather and Space Climate*, 4, A11. <https://doi.org/10.1051/swsc/2014008>
- Welling, D. (2019). Magnetohydrodynamic Models of B and their use in GIC estimates. Geomagnetically induced currents from the Sun to the power grid. *Geophysical Monograph Series*, 43–65. <https://doi.org/10.1002/9781119434412.ch3>
- Willis, D. M., & Young, L. R. (1987). Equation for the field lines of an axisymmetric magnetic multipole. *Geophysical Journal International*, 89(3), 1011–1022. <https://doi.org/10.1111/j.1365-246x.1987.tb05206.x>
- Yu, Y., Ridley, A. J., Welling, D. T., & Tóth, G. (2010). Including gap region field-aligned currents and magnetospheric currents in the MHD calculation of ground-based magnetic field perturbations. *Journal of Geophysical Research*, 115(A8). <https://doi.org/10.1029/2009ja014869>